ACCSCIENCE PUBLISHING

International Journal of Bioprinting

ACCEPTED PAPER · MAIN TEXT

Selective laser melting porous Tantalum scaffold integrated with nano-MgO/Alginate hydrogel for enhanced osteogenesis and immunomodulation in critical-size bone defect repair

Paper version: Accepted Paper

Accepted Papers are manuscripts accepted for publication, encompassing all changes made following the peer review process, along with a standard cover page indicating the paper version and an "Accepted Paper" watermark, but excluding any other editing, typesetting or other changes made by AccScience Publishing and/or authors post-acceptance.

Article ID: IJB026190177

Citation: Jiao H, Xie Q, Cao F, *et al*. Selective laser melting porous Tantalum scaffold integrated with nano-MgO/Alginate hydrogel for enhanced osteogenesis and immunomodulation in critical-size bone defect repair. *Int J Bioprint*. 2026. doi: 10.36922/IJB026190177

Copyright: © 2026 Author(s). This is an Open Access article distributed under the terms of the Creative Commons Attribution License, permitting distribution, and reproduction in any medium, provided the original work is properly cited.

Publisher's Note: AccScience Publishing remains neutral with regard to jurisdictional claims in published maps and institutional affiliations.

AccScience Publishing
RESEARCH ARTICLE
Volume X Issue X (2026)
doi: 10.36922/IJB026190177

Selective laser melting porous Tantalum scaffold integrated with nano-MgO/Alginate hydrogel for enhanced osteogenesis and immunomodulation in critical-size bone defect repair

Running title: Porous Ta scaffold for bone regeneration

Haolin Jiao†, Qinwen Xie†, Fang Cao, Xiao Lin, Bing Ge, Pinqiao Yi, Liqun Song, Haiyao Wang, Lingpeng Liu, Junlei Li*, and Dewei Zhao*

Department of Orthopedics, Affiliated Zhongshan Hospital of Dalian University

†*These authors contributed equally to this work.*

***Corresponding authors:**
Junlei Li (jlli11b@alum.imr.ac.cn)
Dewei Zhao (zhaodewei2016@163.com)

Citation: Jiao H, Xie Q, Cao F, *et al*. Selective laser melting porous Tantalum scaffold integrated with nano-MgO/Alginate hydrogel for enhanced osteogenesis and immunomodulation in critical-size bone defect repair. *Int J Bioprint.* 2026. doi: 10.36922/IJB026190177

Received: May 7, 2026
Revised: June 15, 2026
Accepted: June 22, 2026
Published online: June 22, 2026

Copyright: © 2026 Author(s). This is an Open-Access article distributed under the terms of the Creative Commons Attribution License, permitting distribution, and reproduction in any medium, provided the original work is properly cited.

Publisher's Note: AccScience Publishing remains neutral with regard to jurisdictional claims in published maps and institutional affiliations.

ACCEPTED PAPER

Abstract

The effective repair of critical-sized bone defects remains a major challenge in bone tissue engineering. While porous tantalum (pTa) scaffolds fabricated by selective laser melting offer excellent mechanical compatibility and structural stability, their inherent biological inertness limits further osteogenic outcomes. This study aimed to develop a functionally enhanced composite scaffold by filling 3D-printed porous tantalum with an alginate hydrogel incorporated with nano-magnesium oxide (MgO) particles (pTa@SA-MgO). The hydrogel acted as a carrier for controlled Mg^{2+} ion release. Comprehensive in vitro and in vivo evaluations revealed that this composite scaffold significantly promoted osteogenic activities, including MC3T3-E1 cell proliferation, migration, adhesion, and differentiation (as evidenced by increased ALP activity, mineralized nodule formation, and upregulation of Runx2, OCN, OPN, and Col I gene expression). Moreover, it modulated the immune microenvironment by enhancing M2 macrophage polarization and suppressing the M1 phenotype. In a rabbit femoral defect model, the pTa@SA-MgO scaffold demonstrated superior bone regeneration compared to controls, with greater bone volume (BV/TV) and enhanced new bone formation. This research successfully integrates a sustained ion release strategy with a high-performance metallic scaffold, providing new insights into the design of bone repair materials with synergistic mechanical support and bioactive functionality.

***Keywords**:* 3D-printed porous tantalum; Nano-magnesium oxide; Sodium alginate hydrogel; Bone defect

ACCEPTED PAPER

1. Introduction

The repair of critical-sized bone defects has long remained one of the major challenges in the field of bone tissue engineering [1]. Autografts and allografts are currently the most commonly used clinical treatments; however, their application in the repair of critical-sized bone defects is significantly limited by donor shortage, surgical trauma, immune rejection, and the risk of infection [2,3]. With the rapid development of regenerative medicine and materials science, bone tissue engineering has provided new strategies to address these challenges [4]. A wide range of scaffold materials (including metals, ceramics, polymers, hydrogels, and their composites), stem cells (primarily bone marrow mesenchymal stem cells, adipose-derived stem cells, and periosteal stem cells), and bioactive factors (such as cytokines, drugs, and metal ions) have been extensively investigated for the repair of critical-sized bone defects [5-7]. Additive manufacturing technologies have become an ideal approach for the fabrication of tissue engineering scaffolds due to their advantages in personalized customization and the precise construction of complex porous architectures [8]. Metallic materials exhibit excellent overall mechanical properties and are particularly suitable for the repair of critical-sized bone defects in load-bearing sites [9,10]. Among various metallic materials, titanium alloys have attracted considerable attention, and porous titanium alloy scaffolds fabricated by selective laser melting and electron beam melting have been widely studied for bone defect repair [11]. Tantalum (Ta), owing to its unique physicochemical properties and excellent biocompatibility, has been widely applied in bone repair and joint reconstruction [12,13]. Our previous studies demonstrated that, compared with Ti6Al4V, Ta implants induce less stimulation to the surrounding bone tissue and elicit a lower inflammatory response in vivo, resulting in significantly enhanced peri-implant bone regeneration [14].

The elastic modulus of porous tantalum matches that of natural bone, effectively reducing the stress-shielding effect after being implanted, while also demonstrating excellent resistance to corrosion and structural stability[15]. In particular, with the maturation of selective laser melting (SLM) technology, researchers are able to precisely control the pore size, porosity, and geometric architecture of tantalum scaffolds through 3D printing, thereby improving cell adhesion, nutrient transport, and osseointegration. However, a single material is rarely able to simultaneously satisfy all the requirements of an ideal bone tissue engineering scaffold, including biomechanical performance, osteogenic and angiogenic activity, as well as immunomodulatory capacity [16]. Introducing biodegradable fibers or hydrogel fillers into the pores of 3D-printed porous scaffolds to form composite scaffolds—where the fillers can serve as carriers for cells, cytokines, drugs, and other bioactive factors with osteogenic and immunomodulatory functions—has emerged as a promising strategy for achieving large-scale bone tissue regeneration [17,18]. Composite scaffold materials not only optimize the physicochemical properties of scaffolds but also endow them with multiple biological functions, thereby achieving superior overall performance [19]. A large body of literature has focused on the fabrication of composite scaffolds by incorporating various fillers into

ACCEPTED PAPER

3D-printed porous scaffolds, including calcium phosphates (CaPs), silicates, metals, bioactive molecules, collagen, hydrogels, and other organic materials [20].

Among various bioactive agents, metal ions (including Mg^{2+}, Sr^{2+}, Ga^{3+}, Zn^{2+}, etc.) have attracted widespread attention due to their stability, reliability, and cost-effectiveness [21]. Early studies primarily attempted to endow metallic scaffolds with osteogenic, angiogenic, and antibacterial functions by constructing surface coatings containing various metal ions [22]. Most of these metal ions are incorporated into calcium phosphates to form bioactive coatings on metallic scaffolds, from which the ions are released into the peri-implant microenvironment via coating degradation to exert their biological effects [23]. Although this strategy improves the biological activity of metallic scaffolds, the amount of metal ions loaded within the coating is extremely limited, and the coating thickness is typically only a few to several tens of micrometers; consequently, release kinetics studies have shown that the concentration of bioactive metal ions released from coating-functionalized porous metal scaffolds is often far below the optimal range required to exert maximal biological effects [24]. For example, magnesium-containing coatings typically exhibit an average daily Mg^{2+} release of only several parts per million (ppm), which is substantially lower than the optimal concentration of approximately 50 ppm [25].

Among various carriers for bioactive factors, hydrogels exhibit excellent biocompatibility, and their structural and compositional diversity provides suitable spatial architectures and customizable release kinetics for bioactive agent loading [26]. Owing to their wide availability, good biocompatibility, injectability, and gelation capability, hydrogels have been widely employed in controlled release systems for drugs, ions, and growth factors [27]. Their three-dimensional porous network structure not only enables the loading of nano-scale bioactive components but also provides a favorable microenvironment during tissue regeneration [28].

Nano-magnesium oxide (MgO), as a novel bioactive inorganic material, has gained increasing attention due to its excellent biocompatibility, stability, and controllable ion release characteristics [29]. Accumulated evidence indicates that optimal Mg^{2+} concentrations exert regulatory effects on osteoblast behaviors including adhesion, spreading and differentiation. These ions elevate ALP activity and stimulate the expression of key osteogenic markers like Runx2, COL-1 and OCN. Furthermore, Mg^{2+} facilitates vascularization and bone regeneration by tuning the local microenvironment pH and regulating intracellular signaling pathways [30]. In addition, MgO exhibits intrinsic antibacterial and anti-inflammatory properties, which contribute to improving the immune microenvironment at the implantation site and thereby facilitate bone repair [31-33].

On the other hand, embedding nano-MgO particles into alginate hydrogels enables sustained Mg^{2+} ion release, thereby prolonging the duration of bioactivity and avoiding irritation or potential toxicity caused by burst ion release [34]. Therefore, integrating MgO-loaded hydrogels with porous tantalum scaffolds is expected to simultaneously provide mechanical support, controlled ion release, and bioactive regulation [35].

ACCEPTED PAPER

Based on these considerations, this study for the first time constructed a composite scaffold composed of a nano-MgO-loaded hydrogel integrated with a 3D-printed porous tantalum scaffold [36]. Alginate hydrogel served as a carrier for nano-MgO, enabling the release of magnesium oxide into the peri-implant region through alginate degradation, where MgO subsequently degrades in the physiological environment to generate Mg^{2+} ions [37]. By adjusting the loading amount of MgO, the release kinetics of Mg^{2+} ions from the composite scaffold were regulated to achieve concentrations within the optimal range for maximal biological efficacy [38]. This study aims to combine an active ion regulation strategy with high-performance metallic scaffolds to develop a novel bone repair material featuring both mechanical stability and tunable biological functionality, thereby providing experimental evidence and theoretical support for the functional design and clinical translation of bone tissue engineering scaffolds.

2. Materials and methods

2.1. Materials Preparation

The spherical tantalum powder, with a purity of more than 99.95 wt%, was sourced from Stardust Technology Co., Ltd. Porous tantalum samples, featuring a diamond-shaped pore architecture and 75% porosity with an average pore size of around 500 μm, were fabricated using selective laser melting (SLM, Renishaw AM400, UK). The process of printing was carried out on a Ti-6Al-4V substrate in an atmosphere of high-purity argon, with oxygen levels in the chamber kept under 100 ppm. SLM processing was conducted with a laser power set at 260 W, a point distance of 50 μm, an exposure time of 100 μs, a layer thickness of 30 μm, and a hatch spacing of 65 μm. The samples were subjected to a heat treatment at 1100 °C for 2 hours under a vacuum of 10^{-2} Pa after printing, followed by sandblasting to remove Ta powder that hadn't melted. The samples were subjected to ultrasonic cleaning in acetone, absolute ethanol, and ultrapure water for 15 minutes each, and were subsequently dried for additional use. The above SLM fabrication parameters were adopted directly based on our previous studies. The SLM manufacturing process, printing quality, relative density and microstructure of tantalum scaffolds have been systematically characterized and validated in our earlier published works, so relevant repetitive analyses were not performed in this study[39,40]. Samples were prepared in different sizes according to experimental requirements: 10 mm diameter and 3 mm thick discs for release and cell experiments; 4 mm diameter and 8 mm long cylinders for animal experiments; and diameter of 10 mm and height of 15 mm cylinders for mechanical testing.

2.2. Sample Preparation

At room temperature, 0.2 g of sodium alginate (SA) was dissolved in 10 mL of deionized water under magnetic stirring. Subsequently, nano-magnesium oxide (MgO) particles (0 g, 0.8 g,

ACCEPTED PAPER

1.2 g, and 1.6 g) were added to the solution under vigorous stirring. After complete dispersion, 200–400 μL of calcium chloride solution was added to induce pre-crosslinking, and the mixture was further stirred for 10 min at room temperature until a composite hydrogel was formed. The composite hydrogel was then injected into the porous tantalum scaffolds to form composite scaffolds.

Scaffold extracts were obtained by immersing the composite scaffolds in culture medium at a 0.2 g/mL solid–liquid ratio and incubating them on a shaker for three days. The extracts were centrifuged at a speed of 1000 r/min for 5 minutes, and the supernatant was filtered through a 0.22 μm membrane to yield sterile scaffold extracts for further experimentation.

2.3. Material Characterization

The elemental composition and distribution on the scaffold surface were analyzed using scanning electron microscopy (SEM, Hitachi 3500, Japan) equipped with energy-dispersive X-ray spectroscopy (EDS, Oxford X-Max, UK). The elemental composition of dense disc samples was determined using X-ray fluorescence spectroscopy (XRF; Analytical Zetium, Netherlands). Phase composition was analyzed by X-ray diffraction (XRD; Rigaku D/Max 2500, Japan) using Cu Kα radiation (λ = 1.5406 Å). Surface elemental composition and chemical states were characterized by X-ray photoelectron spectroscopy (XPS; Thermo Scientific Escalab 250XI, USA).

The pTa, pTa@SA, and pTa@SA-MgO scaffolds were immersed in phosphate-buffered saline (PBS) at a solid-to-liquid ratio of 0.2 g/mL and incubated at 37 °C under gentle shaking. At predetermined time points, the supernatant was collected and replaced with an equal volume of fresh PBS to continue incubation. The collected solutions were filtered through a 0.22 μm syringe filter and acidified prior to analysis. The concentration of Mg^{2+} ions was quantified using inductively coupled plasma optical emission spectrometry (ICP-OES), and the cumulative Mg^{2+} release was calculated accordingly.

To evaluate the effect of the composite scaffolds on the pH of the surrounding medium under a simulated physiological environment, the scaffolds were immersed in 5 mL of PBS (pH 7.2; Cytiva, USA). The supernatant was collected on days 1, 2, 3, 5, 7, 10, and 14, and an equal volume of fresh PBS was added after each sampling. The pH value of the collected supernatant was measured using a pH meter.

2.4. In Vitro Cell Experiments

2.4.1. Cell Culture

Mouse preosteoblast MC3T3-E1 and monocyte/macrophage RAW264.7 cells from the Cell Bank of the Chinese Academy of Sciences (Shanghai) were used for in vitro experiments. MC3T3-

ACCEPTED PAPER

E1 cells were cultured in complete DMEM/F-12, and RAW264.7 cells in high-glucose DMEM. Both media were supplemented with 10% FBS and 1% penicillin-streptomycin. Cells were incubated at 37 °C, 5% CO_2 with sufficient humidity, and used for experiments after two passages.

2.4.2. Cell Proliferation Assay

MC3T3-E1 was cultured in DMEM/F-12 containing 10% FBS and 1% penicillin-streptomycin at 37 °C/5% CO_2. Cells were passaged/cryopreserved every 2–3 d using 0.25% trypsin. For proliferation detection, CCK-8 was adopted. Cells (5×10^3/well) were seeded in 48-well plates and cultured with sample extracts (prepared per ISO 10993-12:2012, 3 cm^2/mL, 3 d incubation). Medium was renewed every 2 d, and OD values were detected via microplate reader at day 1, 4 and 7.

2.4.3. Osteoblast Viability Assay

On days 1, 4, and 7 after exposure to the extracts, cells were gently rinsed twice with PBS and stained using a Calcein-AM/PI Live/Dead Cell Staining Kit (Dojindo, Japan), followed by imaging under a fluorescence microscope (TXM-500C, Shanghai, China). The staining solution was prepared by adding 2 μL of Calcein-AM and 3 μL of PI to 1 mL of PBS.

2.4.4. Cell Spreading Assay

MC3T3-E1 (2×10^4 cells/well) was seeded in 48-well plates and cultivated with extracts from pTa, pTa@SA and pTa@SA-MgO. Cells collected at 2 h and 24 h were rinsed with PBS twice, fixed by precooled 4% paraformaldehyde under dark surroundings for 15–30 min. After PBS cleaning, 0.1% Triton X-100 was used for 30 min permeabilization before final triple PBS washing.

Each well received 100 μL Abbkine AbFluor594-Phalloidin for 30 min room-temperature staining prior to triple PBS rinsing. Nuclei were stained with Coolaber DAPI for 5 min, washed again, and preserved in PBS. Cellular spreading was visualized via TXM-500C inverted fluorescence microscopy.

2.4.5. Wound Healing Assay

MC3T3-E1 cells ($3–5\times10^5$/well) were cultured overnight in 6-well plates to full confluence. Uniform scratches were made with sterile 200 μL pipette tips; loose cells were washed off by PBS replacement, and samples were incubated with different scaffold extracts.

Reference marks were made on the bottom of the plate to ensure that images were captured at the same locations at each time point. Images were immediately acquired at 0 h as the baseline and subsequently at 6 h and 24 h during continued incubation. At least three randomly selected

ACCEPTED PAPER

fields of view were recorded per well, with a minimum of three technical replicates and three biological replicates for each group.

The acquired images were analyzed using ImageJ software. The region of interest (ROI) was defined based on the wound boundary at 0 h, and the wound width or cell-free area was quantified using the "Wound Healing Tool/MRI Wound Healing" plugin to calculate the wound closure rate.

2.4.6. Immunofluorescence Staining

MC3T3-E1 cells were seeded into 48-well plates at a density of 2×10^4 cells per well and cultured overnight in complete medium. The medium was then replaced with osteogenic induction extracts of pTa, pTa@SA, or pTa@SA-MgO, which were refreshed every 2 days during the culture period.

Alkaline phosphatase (ALP) immunofluorescence staining was performed on day 7. Briefly, the cells were fixed with 4% paraformaldehyde for 15 min, permeabilized with 0.2% Triton X-100 for 20 min, and subsequently blocked with 10% goat serum (Beyotime, Haimen, China) for 20 min. The cells were then incubated with a primary antibody against ALP (Abcam, Cambridge, UK) overnight at 4 °C. After washing with PBS, a fluorescently labeled secondary antibody (Alexa Fluor 488, Abcam, Cambridge, UK) was applied and incubated at room temperature for 60 min in the dark. Following PBS washes, the cell nuclei were counterstained with DAPI (Beyotime, Shanghai, China) for 10 min. Finally, fluorescence images were acquired using a fluorescence microscope, and quantitative analysis was performed using ImageJ software (version 1.51).

2.4.7. Osteogenic Differentiation Assay

Osteogenic medium was formulated with scaffold extracts plus Sigma additives: 50 μg/mL ascorbic acid, 10 mM β-glycerophosphate disodium and 10 nM dexamethasone. MC3T3-E1 cells (8×10^3/well) were planted in 12-well plates. After overnight cultivation, original medium was substituted with three types of induction extracts. Medium dosage was raised to 2 mL at day 3 and 3 mL at day 5, renewed every two days before day 10 and refreshed daily afterwards with light shielding. ALP staining via Solarbio BCIP/NBT kit was carried out on day 7 and 14, with microscopic observation under XD202 optical microscope.

2.4.8. Alizarin Red S Staining

After overnight incubation, MC3T3-E1 (5000 cells/well in 12-well plates) received 1 mL osteogenic extracts from three scaffolds. Medium volume was adjusted to 2 mL on day 3 and 3 mL on day 5, refreshed every two days before day 10 and replaced daily in dark surroundings later.

ACCEPTED PAPER

Mineralized nodules were stained with 2% Alizarin Red S (Beyotime) at day 14/21 and photographed with XD202 optical microscope.

2.4.9. Quantitative Real-Time PCR

qPCR was adopted to detect osteogenic gene expression of MC3T3-E1. Cells (3×10^4/well) were cultured overnight in 6-well plates before medium replacement with three scaffold extracts (2 mL/well). Medium was supplemented to 3 mL at day 5 and 4 mL at day 7, renewed every two days, and refreshed daily starting from day 10. Cell samples collected at day 7 and 14 were subjected to total RNA isolation with AG21022 kit. RNA quantification was completed on a Thermo NanoDrop One device, and reverse transcription into cDNA was implemented via Takara RR047A reagent on an Eppendorf thermal cycler. qPCR was conducted with Takara TB Green Premix on an ABI 7500 Fast Dx instrument. GAPDH served as the housekeeping gene to normalize expression of Runx2, OCN, OPN and Col I; all primers were custom-synthesized by Accurate Biology. The synthesized primers are shown in Table 1.

Table 1 qRT-PCR primer sequences

gene	forward primer sequence （5′–3′）	reverse primer sequence （3′–5′）
GAPDH	GCCTCCTCCAATTCAACCCTT	CCAAATCCGTTCACACCGAC
OCN	GAACAGACAAGTCCCACACAGC	TCAGCAGAGTGAGCAGAAAGAT
OPN	ATCCTTGCTTGGGTTTGCAG	ACTGCCAATCTCATGGTCGT
Runx2	AGCGGACGAGGCAAGAGTTT	AGGCGGGACACCTACTCTCATA
COL-1	CTCCCAGAACATCACCTATCACT	GGAGGTCTTGGTGGTTTTGTATT

2.4.10. Macrophage Immunofluorescence Staining

RAW264.7 macrophages were cultured in high-glucose DMEM supplemented with 10 vol% fetal bovine serum, 1% penicillin–streptomycin, and 1% sodium pyruvate. Cells were collected using a cell scraper and passaged or cryopreserved every 2–3 days.

RAW264.7 cells (3×10^4/dish) were seeded in 15 mm confocal dishes. After overnight culture, original medium was substituted with 2 mL different scaffold extracts for 48 h incubation. Cells were PBS-rinsed, fixed with pre-cooled 4% paraformaldehyde on ice in the dark, then permeabilized using 0.3% Triton X-100 and finally blocked with 10% goat serum. Diluted primary antibodies against Arg-1 and CCR7 (1:200, Proteintech) were incubated with cells overnight at 4 °C. Post-PBS rinsing, matching Alexa Fluor 488/594-conjugated secondary antibodies (Abcam, 1:200) were supplemented and kept dark for 2 h at ambient temperature. Nuclei were DAPI-stained after washing, and fluorescent pictures were captured by Zeiss CLSM510 confocal microscope.

ACCEPTED PAPER

2.4.11. Expression of angiogenesis- and macrophage polarization-related genes

qPCR was used to quantify M1/M2 marker gene expression in RAW264.7 macrophages. Cells were cultured in 10 cm dishes to 80% confluence, then treated with 10 mL extracts of pTa, SP2-pTa and SP2-pTa-4% scaffolds. The medium was adjusted to 15 mL on day 4, with daily renewal of fresh extracts. After 7 days of incubation, experiments were carried out as described in Section 2.4.9. GAPDH was used as the internal control. Arg-1 and NRROS were M2 markers, while iNOS and IL-6 were M1 markers. All primers were provided by Accurate Biology, with sequences listed in Table 2.

Table 2. qRT-PCR primer sequences

gene	forward primer sequence (5′–3′)	reverse primer sequence (3′–5′)
GAPDH	GCCTCCTCCAATTCAACCCTT	CCAAATCCGTTCACACCGAC
Arg-1	AGCCAGGGACTGACTACCTT	TTGGGAGGAGAAGGCGTTTG
NRROS	AAGACTGAGCACTGACCCTC	TGTCAGACCAACGTTGAGGAG
INOS	CTGCCAGGGTCACAACTTTACA	AACAGCTCAGTCCCTTCACC
IL-6	GTCCTTCCTACCCCAATTTCCA	TGGTCTTGGTCCTTAGCCAC

2.5. In Vivo Experiments

2.5.1. Establishment of the Rabbit Bone Defect Model

All in vivo animal operations were ethically reviewed and approved by the Animal Welfare and Ethics Committee of Zhongshan Hospital, Dalian University (No. DW2025-008-01). Combined with the findings of preliminary in vitro assays, pTa@SA-MgO scaffolds were set as the experimental group, and conventional pTa scaffolds with stable comprehensive properties were adopted as the control group.

Five-month-old male Japanese white rabbits were selected as experimental animals, with six rabbits allocated to each group. Before surgical operation, all rabbits were weighed and raised adaptively until their physiological status stabilized. General anesthesia was performed via marginal ear vein intravenous injection of 3% pentobarbital sodium at a dosage of 25 mg/kg. After successful anesthesia, the surgical site was shaved and disinfected with povidone-iodine solution. A surgical incision was made to expose the femoral tissue, and a standardized bone defect with a diameter of 3 mm was fabricated using a matched drill bit. Sterilized cylindrical scaffolds (3 mm diameter, 8 mm height) including pTa, pTa@SA and pTa@SA-MgO were implanted into the prepared bone defects. Each group contained six rabbits, which were divided into two observation time points (6 weeks and 12 weeks), with three rabbits sacrificed for sampling at each time node.

ACCEPTED PAPER

Subsequent to implantation, surgical incisions were sutured, and intramuscular gentamicin was continuously administrated for three days to avoid postoperative infection. The postoperative health status of all experimental rabbits was monitored daily. After 6 and 12 weeks of implantation, three rabbits in each group were euthanized respectively, and femoral specimens containing scaffold implants were collected for subsequent biological and morphological analysis.

2.5.2. Micro-computed Tomography (Micro-CT) Analysis

Femoral samples were harvested after euthanasia and fixed in 75 vol% ethanol. Micro-CT (Inveon CT, Siemens) was applied to evaluate peri-implant bone regeneration 6 and 12 weeks after implantation. Scanning parameters: 80 kV, 500 μA, 1000 ms exposure, 1-frame average, binning factor 1, pixel size 9.41 μm, 360° rotation with 180 steps. Images were reconstructed in three dimensions using Inveon Acquisition Workplace software (scaling factor = 2). Bone volume fraction (BV/TV) and trabecular number (Tb.N) were then analyzed quantitatively.

2.5.3. Fluorochrome Labeling

Fluorochrome labeling was implemented before animal euthanasia to dynamically monitor the in vivo osteogenesis process. Specifically, 30 mg/kg alizarin red S (Coolaber) was intramuscularly injected two weeks prior to sample collection. This reagent was pre-dissolved in PBS and sterilized via membrane filtration before use. One week before euthanasia, 25 mg/kg calcein (Coolaber) was delivered through intramuscular administration, which was prepared with PBS containing 2% sodium bicarbonate. Subsequent to micro-CT detection, bone tissues containing implants were isolated and cut using a specialized hard tissue slicer. The harvested specimens underwent gradient ethanol dehydration with a solvent dosage 50 times the sample volume. A series of ethanol concentrations (75%, 85%, 95%, and 100%) were applied for 10 days each, with the ethanol solution renewed every 48 hours. Following complete dehydration, non-decalcified hard tissue sections were fabricated through continuous grinding and polishing procedures. Ultimately, a fluorescence microscope was utilized to observe and capture images of the fluorochrome distribution, enabling comparative analysis of new bone growth across different experimental groups at various stages.

2.5.4. Van Gieson Staining

Van Gieson (VG) histochemical staining was carried out on polished non-decalcified hard tissue slices. Specimens were incubated with Servicebio toluidine blue at 60 °C over 15 min and washed with isothermal distilled water. Afterwards, sections were submerged in acid fuchsin

ACCEPTED PAPER

(Macklin) for 10 min under ambient temperature, with anhydrous ethanol applied to achieve proper color differentiation. Prepared slices were then photographed under microscopy.

2.5.5. Hematoxylin and Eosin (H&E) Staining

Peri-implant bone tissues were trimmed into 1–2 mm fragments and decalcified in 10% EDTA solution (Coolaber). The decalcifying liquid was prepared at a 10:1 liquid-to-tissue ratio and tuned to pH 7.3 with sodium hydroxide (Macklin); the EDTA medium was renewed every two days throughout the two-month decalcification period. Specimens underwent stepwise ethanol dehydration (75%, 85%, 95%, 100%, one day per gradient), xylene transparency (Damao AR, 7 h), overnight paraffin infiltration plus another 4 h immersion in fresh paraffin for embedding. Obtained paraffin slices went through drying, deparaffinization and rehydration. After incubation inside a moist box, samples received 10 s hematoxylin staining (Servicebio) at ambient temperature and 20 min running tap water washing, followed by 15 s eosin counterstain (Servicebio). Serial dehydration, transparency and sealing were performed afterwards, and finished slices were visualized and photographed with optical microscope.

2.5.6. Immunohistochemistry (IHC)

The paraffin sections were deparaffinized and rehydrated, then processed with a universal two-step immunohistochemistry detection kit (mouse/rabbit enhanced polymer detection system; ZSGB-BIO, PV-9000) following the instructions provided by the manufacturer. The sections were respectively treated with primary antibodies for osteocalcin (OCN; Thermo Fisher, 10 μg/mL) and type I collagen (Col I; Proteintech, 1:200). Subsequently, freshly prepared diaminobenzidine (DAB) substrate solution (ZSGB-BIO, ZLI-9017) was added and incubated at room temperature for 5–8 min to visualize immunoreactivity. Hematoxylin was used for nuclear counterstaining for 20 seconds, then briefly differentiated in a 1% hydrochloric acid–ethanol solution, followed by a 2-minute rinse under running tap water. Following dehydration, clearing, and mounting, the sections were prepared for microscopic observation. Images were subsequently obtained using an optical microscope.

2.5.7. Immunofluorescence Staining of Paraffin Sections

Paraffin sections were treated with ultraviolet light for at least 4 hours to remove any remaining autofluorescence. After deparaffinization and rehydration, they were blocked with goat serum and permeabilized with 0.1% Triton X-100 for an hour. After applying primary antibodies against CCR7 and arginase-1 (Arg-1) diluted 1:50 in PBS, the sections were incubated overnight at 4 °C in a humidified chamber. They were then washed in PBS on a shaker the following day.

ACCEPTED PAPER

Following the washing step, sections incubated with the Arg-1 primary antibody were exposed to a goat anti-rabbit IgG H&L secondary antibody linked to Alexa Fluor 488 (1:50; Abcam). After incubation with the CCR7 primary antibody, sections were treated with a goat anti-rabbit IgG H&L secondary antibody linked to Alexa Fluor 594 (1:50; Abcam) and kept in the dark at room temperature for 2 hours. After washing with PBS, the sections were stained with DAPI for 10 minutes in darkness. Subsequent PBS washes were done before dehydration and mounting, and images were obtained using a fluorescence microscope (TFM680, Nikon).

2.6. Statistical analysis

GraphPad Prism 9 software (GraphPad Software, USA) was used for all statistical analyses, while ImageJ software (v1.54p) was employed for image quantification. The quantitative data are shown as mean ± standard deviation (SD). The differences between groups were analyzed using a two-way ANOVA (n = 3) or a one-way ANOVA (n = 3), with Tukey's post hoc test applied afterward. A P-value below 0.05 indicated statistical significance. Statistical significance levels are shown in the figures as: "*" for $p < 0.05$, "**" for $p < 0.01$, "***" for $p < 0.001$, "****" for $p < 0.0001$, and "ns" for no significant difference.

3. Results

3.1. Material Characterization

Figure 1a shows sodium alginate hydrogels containing different concentrations of MgO (0 wt%, 8 wt%, 12 wt%, and 16 wt%) and the corresponding composite scaffolds formed after infiltration of the hydrogels into the pores of porous tantalum (pTa) scaffolds. Figure 1b presents the compressive stress–strain curves of the pTa scaffold and pTa@SA-12MgO. The compressive yield strengths of the two scaffolds were 41.5±1.6 MPa and 40.9±2.0 MPa, respectively, with no significant difference between them. The infiltration of MgO-containing sodium alginate hydrogel hardly alters the scaffold's mechanical performance. Figures 1c–f display the microstructures of the composite scaffolds composed of porous tantalum infiltrated with sodium alginate hydrogels containing different concentrations of nano-sized MgO. The MgO-loaded sodium alginate hydrogels completely filled the interconnected pores of the porous tantalum scaffold. Energy-dispersive spectroscopy (EDS) analysis (Figures 1g–j) revealed that the magnesium content in the hydrogels increased markedly with increasing MgO loading. The Mg weight percentages in the pTa@SA–8 wt% MgO, pTa@SA–12 wt% MgO, and pTa@SA–16 wt% MgO groups were 21.74%, 26.50%, and 37.31%, respectively. Elemental mapping results (Figure 1k) further

ACCEPTED PAPER

demonstrated a homogeneous distribution of O, Mg, Ta, and Ca elements on the surface of the composite scaffolds, with no evident elemental aggregation.

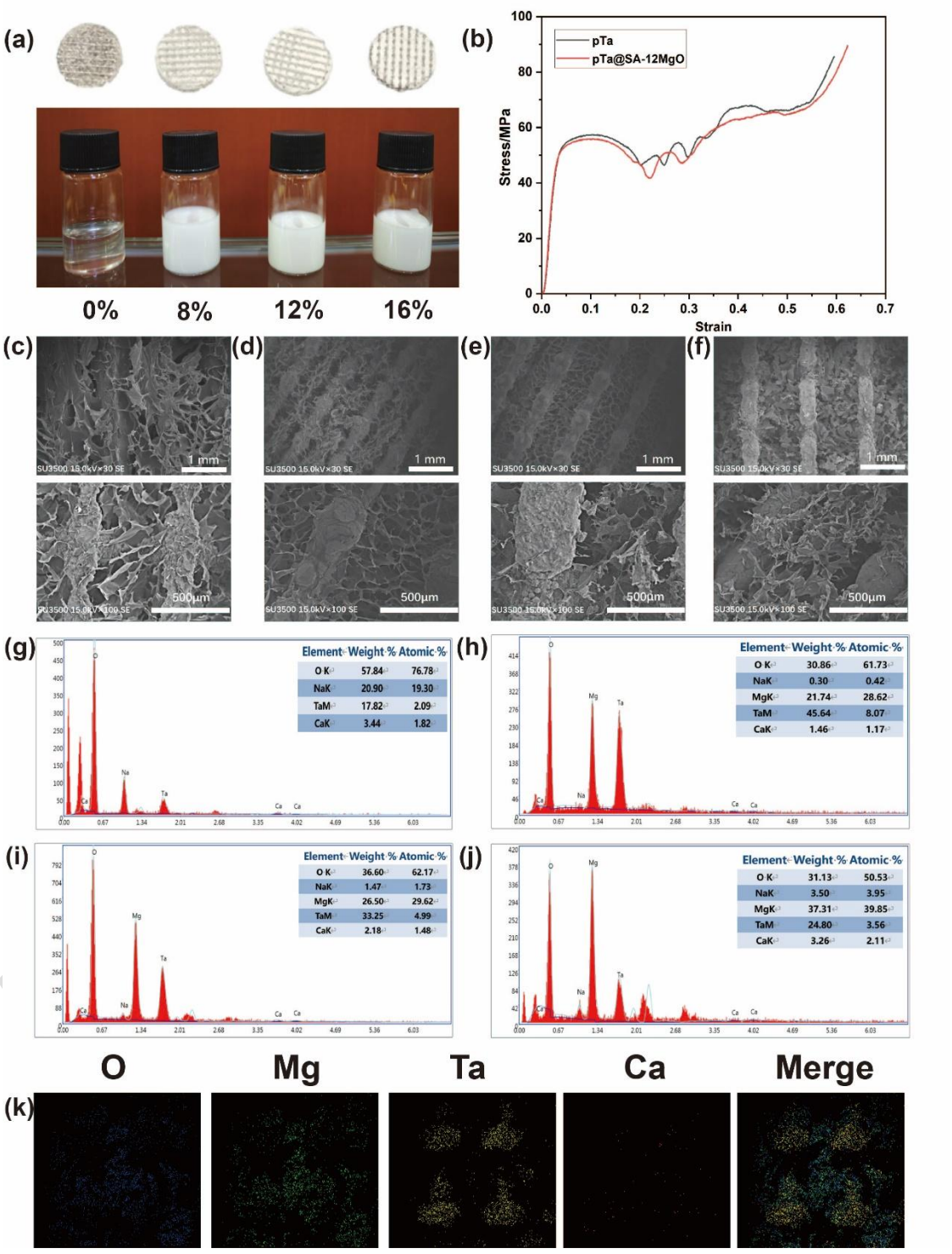


Figure 1. Microstructure and hydrogel property characterization of composite scaffolds. (a) Photographic images of the pTa@SA-MgO hydrogel and the corresponding composite scaffold;

(b) Compressive stress–strain curves of the pTa scaffold and the pTa@SA-12MgO scaffold; (c–f) Representative SEM images of the pTa@SA, pTa@SA-8MgO, pTa@SA-12MgO, and pTa@SA-16MgO scaffolds, respectively, at low and high magnifications; (g–j) Corresponding EDS spectra and elemental compositions of the pTa@SA, pTa@SA-8MgO, pTa@SA-12MgO, and pTa@SA-16MgO scaffolds, respectively; (k) elemental mapping results of the composite scaffolds.

Figure 2a displays the XRD spectra of pure porous Ta scaffolds and their surface-modified composite counterparts. Apart from the characteristic diffraction signals of Ta, newly emerged peaks assigned to sodium alginate (SA) were clearly observed in the pTa@SA group, confirming the successful fabrication of SA coating on the scaffold surface. For the pTa@SA-MgO group, new diffraction peaks appeared at approximately $2\theta = 43°$ and 62°, which can be indexed to the (200) and (220) crystal planes of MgO (PDF#45-0946), confirming the successful incorporation of MgO. Overall, the formation of the composite coating did not alter the crystal structure of the tantalum substrate, indicating that the scaffold maintained good structural stability.

Figure 2b illustrates the FTIR spectra of pTa@SA and pTa@SA-MgO composite scaffolds. Characteristic absorption peaks derived from O–H stretching and COO^- vibrational modes were detected in both groups, which verified the successful immobilization of sodium alginate on the scaffold substrate. Additional absorption peaks attributed to Mg–OH and Mg–O bonds were observed in the pTa@SA-MgO sample, further verifying the effective incorporation of MgO. During degradation, the pTa@SA-MgO scaffold interacted with the buffer solution, resulting in the sustained release of Mg^{2+} ions from the hydrogel for more than 4 weeks (Figure 2c). Figure 2d shows the pH variations of composite scaffolds with different MgO contents during immersion in PBS for 14 days. The results demonstrated that the MgO-doped scaffold groups (8%, 12%, and 16%) exhibited a rapid increase in pH during the early stage of immersion, reaching a peak around day 3 followed by stabilization, whereas the 0% group without MgO maintained a neutral pH throughout the entire period. These findings indicate that the incorporation of MgO effectively elevated the alkalinity of the system in a concentration-dependent manner. To visually demonstrate the morphological evolution of the composite scaffolds during degradation, representative macroscopic photographs were taken after immersion for 1, 3, and 7 days (Fig. 2e). After 1 day of immersion, the hydrogel phase in each group remained relatively intact and uniformly covered the surface of the porous tantalum scaffold. With prolonged immersion, the hydrogel gradually degraded, resulting in progressive exposure of the underlying porous structure. Despite the gradual degradation of the hydrogel phase, the overall architecture of the porous tantalum scaffolds remained stable without obvious structural collapse, indicating that the metallic tantalum could provide sustained mechanical support throughout the degradation process. These observations were consistent with the sustained Mg^{2+} release behavior and pH variation trends shown in Fig. 2c

ACCEPTED PAPER

and d, suggesting that the gradual degradation of the hydrogel enabled prolonged Mg^{2+} release while preserving the structural integrity of the scaffolds.

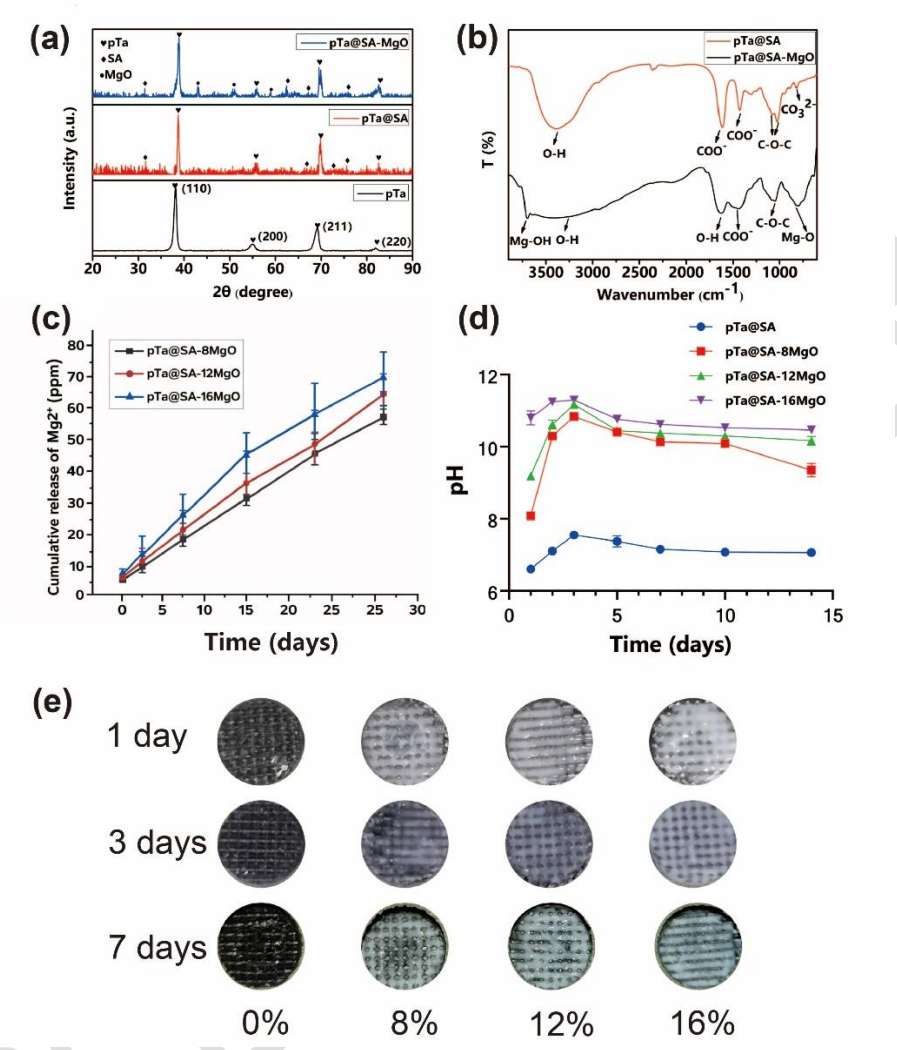


Figure 2. Material characterization of the fabricated composite scaffolds. (a) XRD patterns of different composite scaffold samples; (b) FTIR spectra of the pTa@SA and pTa@SA-MgO composite scaffolds; (c) In vitro Mg^{2+} release behavior of the pTa@SA-MgO scaffold; (d) pH changes of the surrounding environment triggered by composite scaffolds during immersion; (e) Representative macroscopic images of the composite scaffolds during the degradation process.

3.2. In vitro experimental results

As a biomaterial scaffold, favorable biocompatibility is a prerequisite for clinical application. Cell proliferation on pTa@SA, pTa@SA-8MgO, pTa@SA-12MgO, and pTa@SA-16MgO composite scaffolds was evaluated, as shown in Figure 3a, with the pTa@SA group serving as the

control. After one day of incubation, the pTa@SA-8MgO, pTa@SA-12MgO and pTa@SA-16MgO groups displayed significantly enhanced cell viability compared with the control group ($p < 0.05$). With the culture duration extended to day 3, cellular viability was elevated across all experimental groups. Notably, the pTa@SA-12MgO group yielded the maximum optical density (OD) value, which was statistically higher than that of the control group ($p < 0.01$).Moreover, both the pTa@SA-8MgO and pTa@SA-12MgO groups showed markedly enhanced proliferation compared with the control (**$p < 0.0001$). On day 7, cell proliferation was further enhanced in all MgO-containing groups, which exhibited significantly higher viability than the control group (**$p < 0.0001$). Among them, the pTa@SA-12MgO group demonstrated the most pronounced proliferative effect and was significantly superior to both the pTa@SA-8MgO and pTa@SA-16MgO groups (**$p < 0.0001$). Collectively, these results indicate that the incorporation of MgO effectively promotes cell proliferation, with the pTa@SA-12MgO scaffold showing the optimal performance; therefore, this formulation was selected for subsequent experiments.

Live/dead staining (Figure 3b) confirmed high viability of MC3T3-E1 cells treated with various scaffold extracts, with negligible dead cells observed in all groups and good material biocompatibility verified. The pTa@SA-12MgO group exhibited distinctly stronger cell proliferation at day 4 and day 7 than pTa and pTa@SA groups.

Figure 3c illustrates the cell spreading morphology and cytoskeletal fluorescence intensity, while Figure 3f presents the corresponding quantitative analysis. At 2 h, no significant differences in cell spreading were observed among the groups. In contrast, at 24 h, the cytoskeletal fluorescence intensity of the pTa@SA-12MgO group was approximately 1.5-fold higher than that of the pTa group, indicating a superior ability to promote cell spreading.

Figure 3d depicts osteoblast migration in response to different scaffold extracts. Cells steadily filled the scratched area during culture, with the pTa@SA-MgO group showing the best wound closure. Group differences were not significant at 6 h (Figure 3e). The pTa@SA-MgO group exhibited the fastest migration at 24 h, verifying the promotive effect of MgO on osteoblast migration.

ACCEPTED PAPER

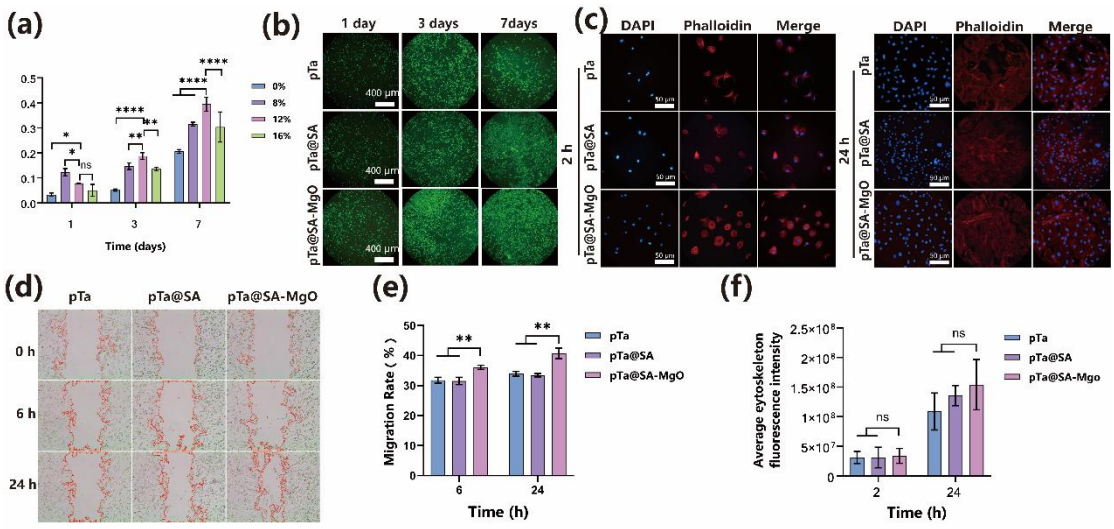


Figure 3. Cell adhesion, proliferation and migration upon treatment with different scaffolds. (a) CCK-8 of MC3T3-E1 cells cultured with extracts from MgO-containing alginate/Ta scaffolds for 1, 4 and 7 days; (b) Live/dead fluorescence imaging of MC3T3-E1 cells at different culture times; (c) Phalloidin and DAPI staining of cells treated with three types of scaffold extracts for 2 h and 24 h; (d) Scratch wound images of MC3T3-E1 cells at 0, 6 and 24 h; (e) Statistical results of cell migration rates from (d); (f) Mean fluorescence intensity of cell cytoskeleton.

ALP expression in the early stage and extracellular matrix mineralization are typical indicators of cell osteogenic differentiation on material surfaces. Immunofluorescence staining was performed to detect ALP distribution. ALP expression was observed in all groups at day 7 (Figure 4a), and the pTa@SA-12MgO group exhibited the highest ALP level. Quantitative analysis (Figure 4c) showed highly significant differences between pTa@SA-12MgO and the other two groups ($p < 0.0001$).

Based on the screening results, the selected SP2-pTa-4% group was further investigated for its osteogenic potential. ALP staining and ARS staining were separately applied to assess the early and late stages of osteogenic differentiation. As shown in Figure. 4e and the corresponding quantitative analysis performed using ImageJ (v1.54p) (Figure. 4f), the pTa@SA-12MgO group exhibited a 2.1-fold increase in early-stage osteogenesis and a 1.1-fold enhancement in late-stage osteogenesis compared with the pTa group. Meanwhile, the pTa@SA group displayed comparable results to the pTa group. ALP activity was used to assess early osteogenic differentiation, while ARS staining was employed to evaluate late-stage mineralization. As illustrated in Figure. 4b, the pTa@SA-12MgO group demonstrated a pronounced promotive effect on both early and late osteogenic differentiation.

ACCEPTED PAPER

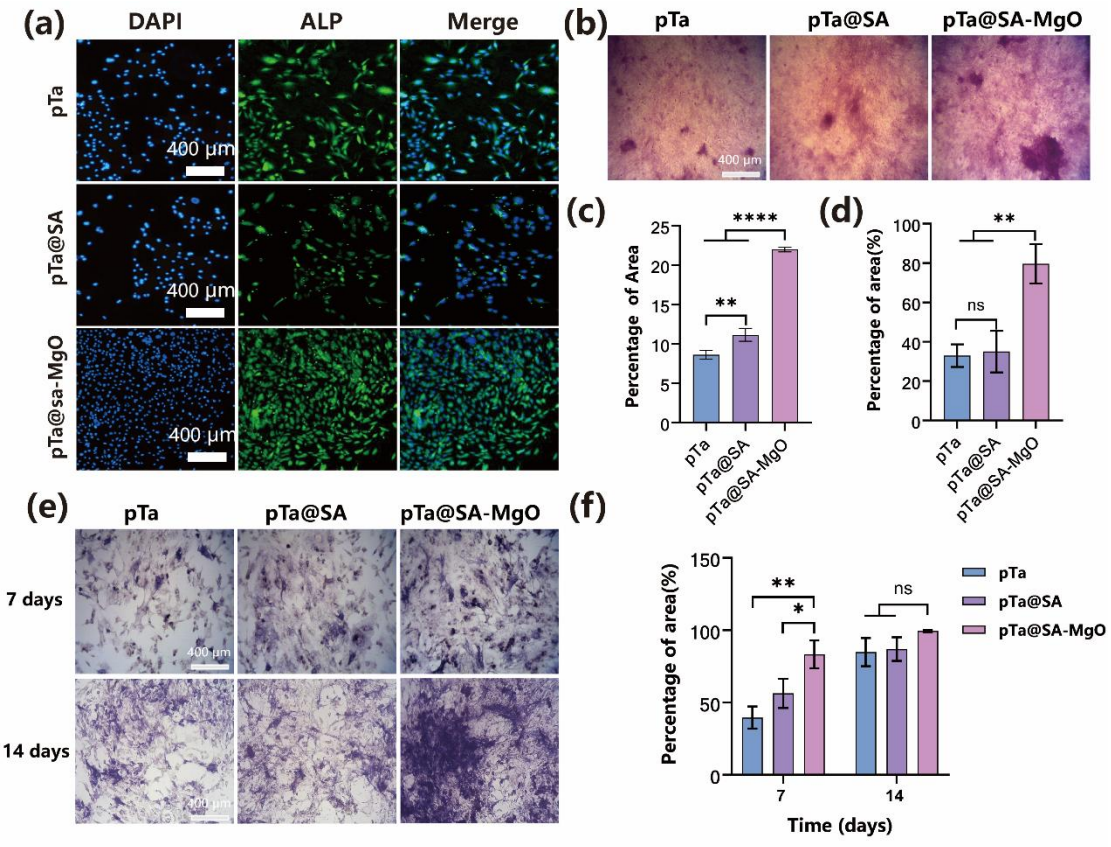


Figure 4. Osteogenic differentiation performance of MC3T3-E1 cells cultured with scaffold extracts. (a) Immunofluorescent staining of ALP in MC3T3-E1 cells after 7 days of incubation with different extraction media; (b) ARS staining results of MC3T3-E1 cells after 21 days of osteogenic induction using pTa, pTa@SA and pTa@SA-MgO scaffold extracts; (c) Quantitative statistics of ALP-positive areas corresponding to the immunofluorescence images in (a); (d) Quantitative analysis of mineralized matrix areas based on the ARS staining results in (b) at day 21; (e) ALP staining of MC3T3-E1 cells after 7 and 14 days of osteogenic culture with different scaffold extracts; (f) Quantitative comparison of ALP-positive areas obtained from the staining images in (e) at day 7 and day 14.

Gene expression in MC3T3-E1 cells at day 7 and day 14 is shown in Figure 5a and 5b. The pTa@SA-12MgO group significantly upregulated all osteogenic genes. The pTa group moderately enhanced gene expression on day 7, while obvious differences from pTa@SA-12MgO remained on day 14, which is consistent with prior studies about pure tantalum. The pTa@SA group showed limited osteogenic activity at both time points. All these data are consistent with ALP and ARS staining results.

Figure 5d includes immunofluorescence images and quantitative analysis of M2 marker Arg-1 and M1 marker CCR7. The pTa group showed weak anti-inflammatory activity, as documented

in previous studies. In pTa@SA-12MgO, Arg-1 fluorescence intensity was ~1.4 times that of pTa, and CCR7 intensity decreased to ~0.3 times, proving efficient inhibition of M1 polarization and good anti-inflammatory effects. The pTa@SA group inhibited both macrophage phenotypes, with stronger suppression on M1 cells. Since CCR7 expression was higher than Arg-1, this group still had a slight pro-inflammatory trend. Quantitative data are presented in Figure 5e.

Analysis of macrophage-related gene expression results (Figure 5c) revealed that the pTa@SA-12MgO group exhibited partial suppression of pro-inflammatory gene expression while more strongly promoting the expression of anti-inflammatory genes in macrophages. The other two groups showed only slight increases or decreases in relative gene expression levels, and overall, the pTa group demonstrated a relatively weak inhibitory effect on inflammation. Although the pTa@SA group showed a certain reduction in pro-inflammatory gene expression, its overall gene expression profile still suggested a relatively pronounced pro-inflammatory tendency. By comparing the effects of different experimental groups on macrophage differentiation, it is evident that the incorporation of magnesium ions markedly promoted polarization toward the anti-inflammatory phenotype. Previous studies have also reported the anti-inflammatory effects of magnesium ions; however, the underlying mechanisms remain to be further elucidated.

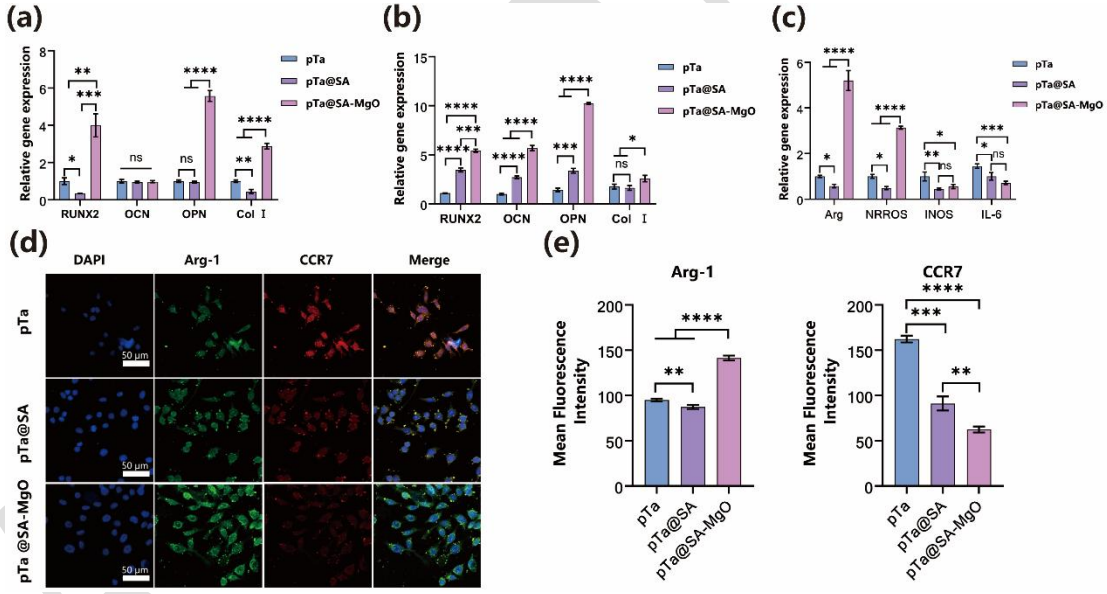


Figure 5. Cell responses to different scaffolds. (a, b) Relative osteogenic gene expression in MC3T3-E1 cells at 7 and 14 days. (c) Expression of macrophage polarization genes in RAW264.7 cells after 7 days of treatment. (d) Immunofluorescence staining of RAW264.7 cells cultured with scaffold extracts for 48 h. (e) Quantitative analysis of red and green fluorescence intensity in (d).

3.3. In vivo experimental results

A rabbit femoral bone defect model was reliably constructed in this study, and no postoperative infection or mortality occurred during the 6-week and 12-week observation periods. All experimental rabbits survived the entire study process, and all implanted scaffolds remained stable without loosening throughout the implantation cycle. All specimen samples were successfully collected at the scheduled time points. Micro-CT reconstructed images of femoral samples at 6 and 12 weeks after implantation are displayed in Figure 6a and 6b. Quantitative Micro-CT analysis demonstrated that the pTa@SA-12MgO group possessed a higher bone volume fraction than the pure pTa group at both detection time points. At 12 weeks post-surgery, the bone volume fraction of the pTa@SA-12MgO group was approximately 1.2-fold higher than that of the pTa group (Figure 6c, d). Van Gieson (VG) staining of hard tissue sections further validated the bone regeneration performance of different scaffolds (Figure 6e). The pTa@SA-12MgO group exhibited significantly enhanced bone ingrowth behavior, with its newly formed bone area reaching roughly 1.4 times that of the pTa group. Particularly, at 12 weeks after implantation, new bone tissues grew inward across the scaffold structure and formed partial interconnected bone networks (Figure 6f).

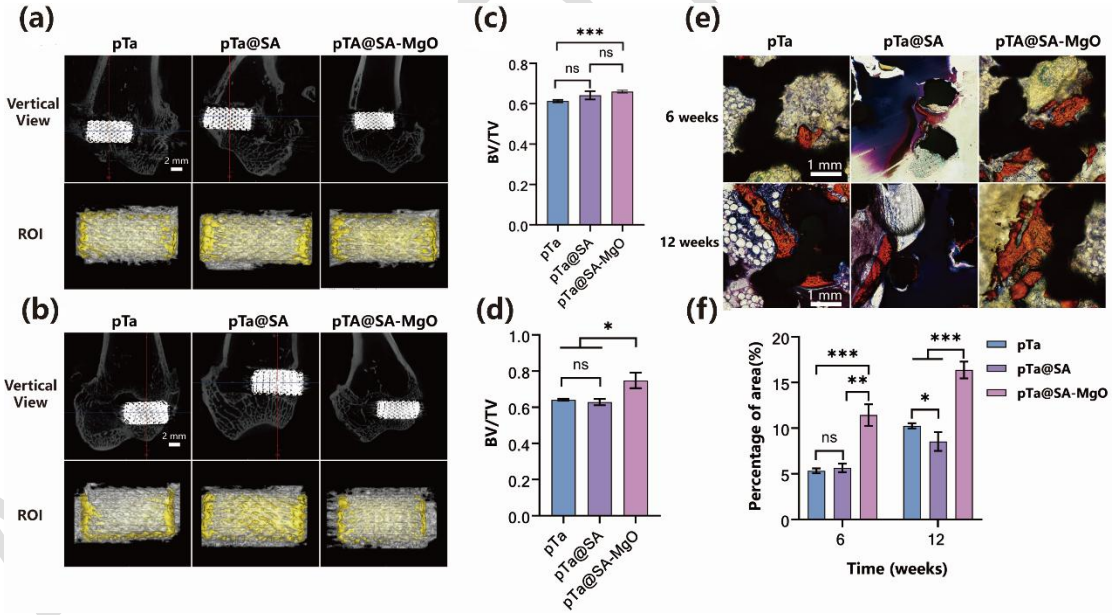


Figure 6. In vivo bone regeneration assessment of different scaffolds based on a rabbit femoral implantation model at 6 and 12 weeks postoperatively. (a, b) Typical Micro-CT reconstruction images of scaffold implantation regions at two healing stages; (c, d) Quantitative statistics of trabecular number per unit length calculated from Micro-CT scanning data; (e) Van Gieson (VG) staining results of hard tissue sections harvested from the implantation sites; (f) Morphometric analysis of the proportion of newly formed bone area (red-stained areas) corresponding to the staining images in (e).

The osteogenic mineralization capacity of different scaffolds was evaluated by analyzing the spacing between labeled lines at two different time points. Calcium nodule deposition was observed in all three experimental groups (Figure 7a), and the results confirmed that the pTa@SA-12MgO group possessed a faster bone formation rate than the pTa group at identical culture stages. Immunohistochemical staining was further performed to detect the expression of osteogenic markers (Figure 7c). At both postoperative time points, the pTa@SA-MgO group displayed remarkably stronger positive staining of OCN and Col I compared with the pTa group. Specifically, the positive expression areas of OCN and Col I in the pTa@SA-MgO group were 1.4-fold and 1.8-fold higher than those in the pTa group, respectively (Figure 7d). Collectively, these findings demonstrate that the pTa@SA-MgO scaffold possesses outstanding in vivo osteogenic performance and can effectively promote bone regeneration.

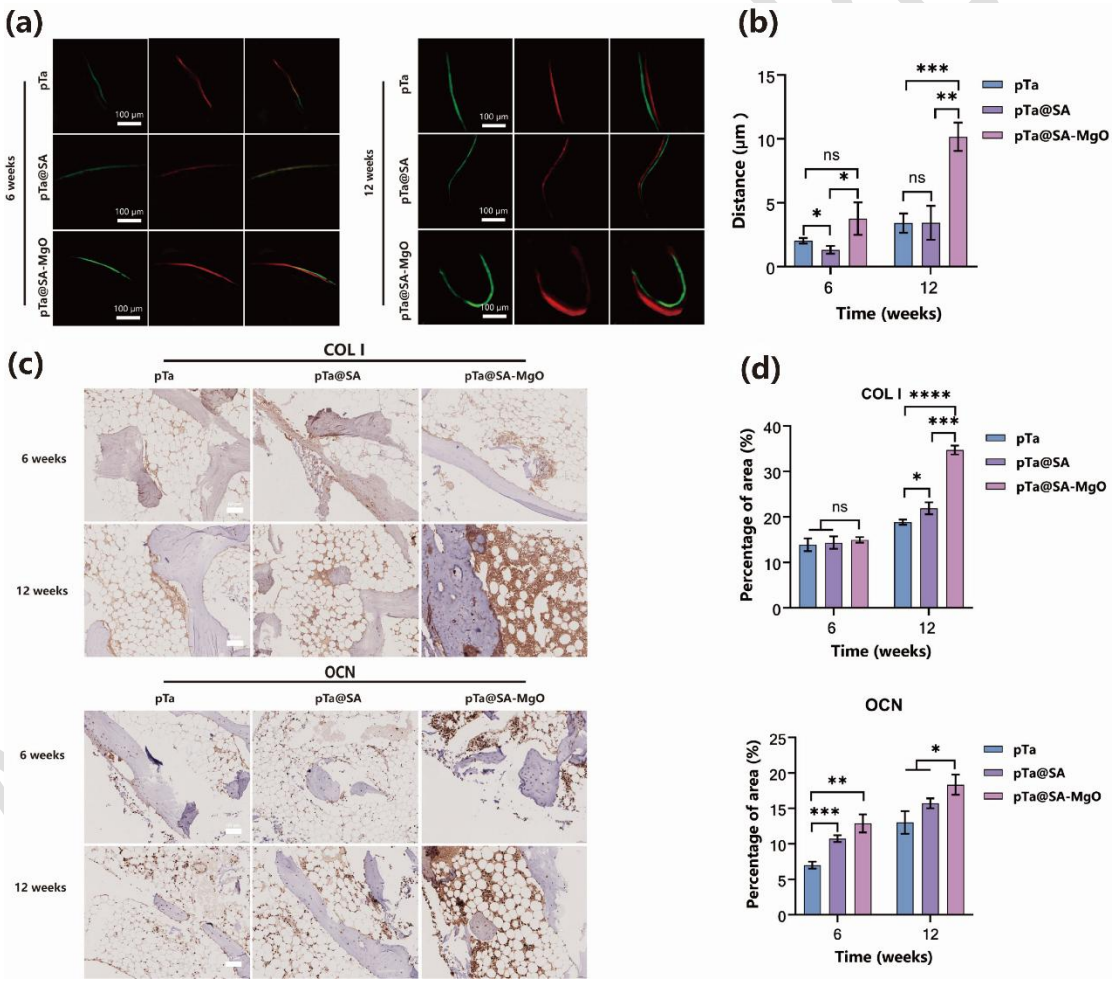


Figure 7. In vivo bone regeneration evaluation of different scaffolds in rabbit implantation models after 6 and 12 weeks of healing. (a) Fluorescent labeling imaging for visualization of newly regenerated bone tissues; (b) Statistical analysis of bone formation rates in the pTa, pTa@SA and pTa@SA-MgO groups; (c) Immunohistochemical staining of tissue sections

collected at two postoperative time points; (d) Semi-quantitative quantification of the positive brown-stained areas derived from the immunohistochemical images in (c).

Figure 8a presents the immunofluorescence staining results of key inflammatory biomarkers. At the two detected time points, the fluorescence intensity of the M2 macrophage marker Arg-1 was significantly upregulated in the pTa@SA-MgO group, reaching 2.2-fold of that in the pTa group. In contrast, the fluorescence level of the M1 macrophage marker CCR7 was downregulated, declining to half of the value obtained from the pTa group (Figure 8b). These outcomes verify that the pTa@SA-MgO scaffold possesses superior anti-inflammatory properties. Additionally, H&E staining was conducted for histological observation of tissues surrounding the implants (Figure 8c). The morphological characteristics of periprosthetic soft tissue and bone tissue can effectively reflect the local microenvironment during bone regenerative repair. Compared with the pTa and pTa@SA groups, the pTa@SA-MgO group exhibited reduced inflammatory cell infiltration and a lower degree of inflammatory response. In conjunction with the immunohistochemical and immunofluorescence findings, these results suggest that the composite scaffold can, to a certain extent, modulate the local immune microenvironment and suppress excessive inflammatory responses, thereby providing more favorable conditions for bone regeneration.

Specifically, as the implantation time increased, the osteogenic effect of the pTa@SA-MgO group continued to enhance, indicating that this material has good potential in promoting bone tissue regeneration and repair.

ACCEPTED PAPER

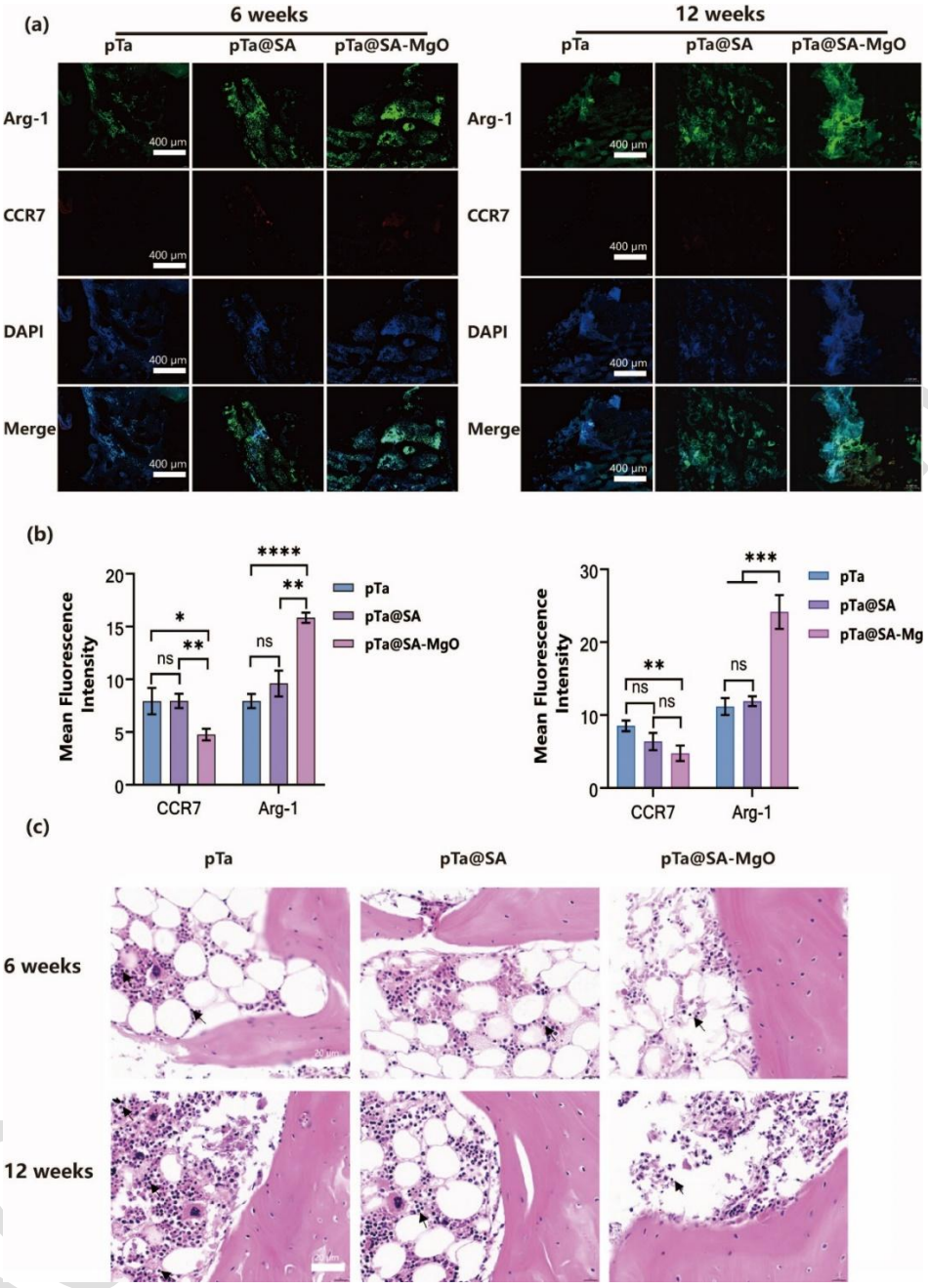


Figure 8. Inflammatory response assessment of biomaterial implantation sites in a rabbit model. (a) Representative immunofluorescence micrographs of peri-implant tissues collected at 6 and 12 weeks after scaffold implantation; (b) Quantitative detection of green and red fluorescence signal intensities based on the immunofluorescence images in (a); (c) H&E histological staining of peri-implant tissues at the two postoperative time points.

4. Discussion

This study successfully developed a composite scaffold (pTa@SA-MgO) consisting of magnesium oxide (MgO)-loaded sodium alginate hydrogel and 3D-printed porous tantalum, and systematically evaluated its overall performance in large bone defect repair. The results show that this composite scaffold not only inherits the excellent mechanical properties and biocompatibility of porous tantalum but also achieves controlled release of magnesium ions via the hydrogel carrier, demonstrating significant advantages in promoting osteoblast proliferation, migration, differentiation, and modulating the immune microenvironment[32,33].

The porous tantalum scaffold was prepared using selective laser melting (SLM) technology. Its diamond-shaped pore structure (porosity 75%, pore size 500 μm) not only provides sufficient specific surface area for cell adhesion and tissue ingrowth but also, more importantly, its compressive yield strength (37.1±2.5 MPa) and elastic modulus (2.98±0.14 GPa) match those of natural bone tissue, effectively avoiding the common "stress shielding" effect seen with traditional metal implants [12,41,42]. SEM and EDS analyses show that the sodium alginate hydrogel can completely fill the pores of the porous tantalum scaffold, and the magnesium content significantly increases with the addition of MgO. XRD and FTIR results further confirmed the successful incorporation of MgO, laying the foundation for the subsequent realization of biological functions.

In vitro release experiments demonstrated that the pTa@SA-MgO composite scaffold was capable of continuously releasing Mg^{2+} over a period of 28 days, and that the release kinetics could be precisely regulated by adjusting the MgO content. Notably, the pTa@SA-12MgO group maintained the Mg^{2+} concentration within the optimal range for biological activity (approximately 50 ppm) [43], which is markedly superior to conventional surface-coating strategies, where limitations in coating thickness and ion loading often prevent the attainment of therapeutically effective concentrations. For example, magnesium-containing coatings typically release only a few ppm of Mg^{2+} per day, which is far below the ideal concentration range required for biological efficacy [44,45]. Meanwhile, pH monitoring results indicated that the incorporation of MgO moderately increased the alkalinity of the system (pH 10–11), and such a mildly alkaline microenvironment has been demonstrated to be beneficial for osteoblast activity and bone matrix mineralization [46,47].

The cellular experimental results demonstrated that the pTa@SA-MgO composite scaffold exhibited significant advantages in promoting osteoblast activity. CCK-8 and live/dead staining assays revealed that all MgO-containing groups significantly enhanced the proliferation of MC3T3-E1 cells, with the pTa@SA-12MgO group showing the most pronounced effect, indicating that an appropriate concentration of Mg^{2+} exerts a positive regulatory effect on cell growth, which is consistent with previous reports [48,49]. Cytoskeletal staining further demonstrated that the pTa@SA-12MgO group markedly promoted cell spreading, with fluorescence intensity approximately 1.5-fold higher than that of the pTa group. Scratch wound assays further confirmed that the incorporation of MgO effectively enhanced osteoblast migration. Bone repair and

ACCEPTED PAPER

regeneration are complex biological processes that largely depend on the migration of cells, particularly osteoblasts and mesenchymal stem cells (MSCs), toward the defect site. Effective cell migration is critical for successful bone defect repair, as it facilitates the recruitment of key cells involved in bone formation and remodeling to the injury site [50]. Numerous studies have emphasized the importance of cell migration in promoting bone regeneration and have provided insights into potential therapeutic strategies [51,52].

Both ALP immunofluorescence staining and ALP staining results demonstrated that the pTa@SA-12MgO group exhibited a significantly enhanced early osteogenic differentiation, with the ALP-positive area reaching 2.1-fold that of the pTa group. qPCR analysis further confirmed that the expression of key osteogenic genes, including Runx2, OCN, OPN, and Col I, was significantly upregulated in this group, indicating that Mg^{2+} promotes osteogenic differentiation at the transcriptional level. Meanwhile, Alizarin Red S staining revealed that the pTa@SA-MgO composite scaffold also exhibited superior capability in promoting extracellular matrix mineralization, providing strong support for bone formation and maturation in vivo. Magnesium ions synergistically promote osteogenesis through multiple pathways and play a crucial role in maintaining skeletal health [53]. As an essential cofactor for key enzymes such as alkaline phosphatase, Mg^{2+} enhances enzymatic activity and directly participates in hydroxyapatite formation, which is the core component of bone mineralization [54]. At the cellular level, Mg^{2+} stimulates osteoblast proliferation and differentiation, promotes collagen secretion to provide structural support for the bone matrix, and simultaneously suppresses excessive osteoclast activation, thereby maintaining the dynamic balance of bone remodeling [55]. At the molecular level, Mg^{2+} enhances osteogenesis by regulating signaling pathways such as TRPM7/PI3K/AKT, thereby promoting the expression of osteogenesis-related genes [56]. Clinical studies have demonstrated that adequate magnesium intake significantly increases bone mineral density and reduces fracture risk [57]. Collectively, these mechanisms highlight the multifunctional role of Mg^{2+} in bone development and maintenance, underscoring its considerable potential in bone defect repair and regenerative therapies.

Macrophages act as the primary regulators of the early inflammatory response surrounding implanted biomaterials, and their polarization states directly influence the bone regeneration process [58,59]. Immunofluorescence staining and qPCR analyses revealed that the pTa@SA-12MgO group significantly promoted macrophage polarization toward the anti-inflammatory M2 phenotype, with Arg-1 fluorescence intensity reaching 1.4-fold that of the pTa group, while simultaneously suppressing polarization toward the pro-inflammatory M1 phenotype, as evidenced by a reduction of CCR7 fluorescence intensity to 0.3-fold of the pTa group. These findings are consistent with previous reports demonstrating the anti-inflammatory properties of Mg^{2+}, indicating that the composite scaffold effectively improves the local immune

ACCEPTED PAPER

microenvironment at the implantation site through controlled magnesium ion release, thereby creating favorable conditions for subsequent bone regeneration [32,33,48,60,61].

The in vivo experimental results demonstrated that the pTa@SA-MgO composite scaffold exhibited outstanding bone repair capability in a rabbit bone defect model. Micro-CT analysis revealed that after 12 weeks of implantation, the pTa@SA-MgO group showed significantly higher bone volume fraction (BV/TV) and trabecular number compared with the control group. Van Gieson (VG) staining further confirmed a markedly increased extent of bone ingrowth in the pTa@SA-MgO group, with the bone area reaching approximately 1.4-fold that of the pTa group. Fluorochrome labeling analysis showed a pronounced increase in the new bone formation rate in the pTa@SA-MgO group, indicating that the composite scaffold effectively promotes the dynamic process of bone tissue formation.

The novelty of this study is mainly reflected in the following aspects. First, this study overcomes the functional limitations of conventional single-component materials by adopting a composite scaffold design strategy that integrates structural mechanical stability with tunable biological functionality. The porous tantalum scaffold provides robust mechanical support, while the sodium alginate hydrogel serves as an ideal carrier for magnesium ions, enabling their sustained and controllable release. Second, this work addresses a critical limitation of existing technologies, namely the insufficient release concentration of bioactive metal ions. Conventional surface coating approaches are constrained by physical limitations and therefore struggle to maintain therapeutically effective ion concentrations. In contrast, by dispersing nano-sized MgO particles within the hydrogel network, this study markedly enhances ion loading capacity and enables precise regulation of ion release kinetics through adjustment of hydrogel degradation rates and MgO content. Third, the multifaceted biological effects of magnesium ions are comprehensively demonstrated in this study. Beyond its well-established osteogenic effects, magnesium ions were found to exert significant immunomodulatory functions, and this dual-action mechanism is of great importance for the repair of bone defects.

Although this study has yielded encouraging results, several limitations remain that should be addressed in future investigations. First, although pTa@SA-12MgO was identified as the optimal composition in this study, bone defects of different sizes and anatomical locations may require tailored optimization of MgO content and hydrogel formulations to meet personalized therapeutic demands. Second, the precise molecular mechanisms by which magnesium ions regulate macrophage polarization have yet to be fully elucidated. Future studies should focus on clarifying how magnesium ions modulate inflammatory responses through key signaling pathways, such as NF-κB and MAPK, which would provide a deeper theoretical basis for the rational optimization of composite scaffold design. Third, the maximum observation period in this study was limited to 12 weeks, whereas complete regeneration of large-segment bone defects typically requires a longer time course. Therefore, long-term animal studies are necessary to

ACCEPTED PAPER

comprehensively evaluate the long-term safety and stability of the proposed biomaterial system.In summary, the successfully developed pTa@SA-MgO composite scaffold in this study exhibited an excellent overall performance, including robust mechanical support, enhanced osteogenic cellular activity, and effective modulation of the local immune microenvironment. This novel bone repair material not only provides a promising therapeutic strategy for the clinical treatment of large-segment bone defects but also offers new insights into the functional design of bone tissue engineering scaffolds. Future studies should focus on personalized material customization, deeper elucidation of the underlying biological mechanisms, and translational research toward clinical applications, thereby facilitating the progression of this innovative technology from bench to bedside.

5. Conclusion

In this study, a composite scaffold integrating nano-MgO–loaded sodium alginate hydrogel with 3D-printed porous tantalum was successfully developed. The scaffold exhibited favorable structural stability and mechanical support while enabling sustained Mg^{2+} release, which enhanced osteogenic cellular responses and modulated the local biological microenvironment. These findings demonstrate that the pTa@SA-MgO scaffold provides a functional platform combining mechanical reliability with bioactivity for bone regeneration. Although further in vivo validation and long-term evaluation are required, this strategy offers a promising direction for the design of multifunctional metallic scaffolds for large bone defect repair.

Acknowledgments

None.

Funding

This study was funded by the LiaoNing Revitalization Talents Program (project No. XLYC2203102), Science Fund for Distinguished Young Scholars of Dalian (project No. 2024RJ007).

Conflict of interest

The authors declare they have no competing interests.

Author contributions

Conceptualization: Junlei Li, Dewei Zhao

Formal analysis: Xiao Lin, Junlei Li

Investigation: Haolin Jiao, Qinwen Xie, Fang Cao, Pinqiao Yi, Liqun Song, Haiyao Wang, Lingpeng Liu

ACCEPTED PAPER

Methodology: Bing Ge, Junlei Li
Writing–original draft: Haolin Jiao
Writing–review & editing: Junlei Li

Ethics approval and consent to participate

Not applicable.

Consent for publication

Not applicable.

Availability of data

Data are available from the corresponding author upon reasonable request.

References

1. Xu W, Gao W, Zhang Y, et al. Injectable HAMA-CPC hydrogels loaded with high-yield 3D bioprinted adipose-derived stem cell small extracellular vesicles for increased bone repair. *J Nanobiotechnology*. Jul 21 2025;23(1):531. doi:https://pubmed.ncbi.nlm.nih.gov/40685362/
2. Gao C, Qiu Z-Y, Hou J-W, et al. Clinical observation of mineralized collagen bone grafting after curettage of benign bone tumors. *Regen Biomater*. 2020;7(6):567–575. doi:10.1093/rb/rbaa031
3. Zhu W, Li C, Yao M, et al. Advances in osseointegration of biomimetic mineralized collagen and inorganic metal elements of natural bone for bone repair. *Regen Biomater*. 2023;10doi:10.1093/rb/rbad030
4. Song Y, Wang N, Shi H, et al. Biomaterials combined with ADSCs for bone tissue engineering: current advances and applications. *Regen Biomater*. 2023;10doi:10.1093/rb/rbad083
5. Su X, Wei L, Xu Z, et al. Evaluation and Application of Silk Fibroin Based Biomaterials to Promote Cartilage Regeneration in Osteoarthritis Therapy. *Biomedicines*. Aug 10 2023;11(8)doi:10.3390/biomedicines11082244
6. Goncharov EN, Koval OA, Nikolaevich Bezuglov E, et al. Conservative Treatment in Avascular Necrosis of the Femoral Head: A Systematic Review. *Med Sci (Basel)*. Jul 2 2024;12(3)doi:10.3390/medsci12030032
7. Wei Y, Lyu P, Bi R, et al. Neural Regeneration in Regenerative Endodontic Treatment: An Overview and Current Trends. *Int J Mol Sci*. Dec 7 2022;23(24)doi:10.3390/ijms232415492
8. Lu Y, Deshmukh S, Jones I, Chiu YL. Biodegradable magnesium alloys for orthopaedic applications. *Biomater Transl*. 2021;2(3):214–235. doi:10.12336/biomatertransl.2021.03.005
9. Yu L, Sun F, Wang Y, et al. Effects of MgO nanoparticle addition on the mechanical properties, degradation properties, antibacterial properties and in vitro and in vivo biological properties of 3D-printed Zn scaffolds. *Bioact Mater*. Jul 2024;37:72–85. doi:10.1016/j.bioactmat.2024.03.016
10. Cao B, Xie L, Xu Y, et al. Dual-core-component multiphasic bioceramic granules with selective-area porous structures facilitating bone tissue regeneration and repair. *RSC Adv*. Mar 26 2024;14(15):10526–10537. doi:10.1039/d4ra00911h
11. Jaeyoung R, Kang HS, Kang BH, et al. Effect of rhBMP-2 applied with a 3D-printed

ACCEPTED PAPER

titanium implant on new bone formation in rabbit calvarium. *J Appl Oral Sci*. 2021;29:e20201092. doi:10.1590/1678-7757-2020-1092
12. Gao H, Yang J, Jin X, et al. Static Compressive Behavior and Failure Mechanism of Tantalum Scaffolds with Optimized Periodic Lattice Fabricated by Laser-Based Additive Manufacturing. *3D Print Addit Manuf*. Oct 1 2023;10(5):887–904. doi:10.1089/3dp.2021.0253
13. Mao S, Liu Y, Wang F, et al. Design and biomechanical analysis of patient-specific porous tantalum prostheses for knee joint revision surgery. *IJB*. 9(4)doi:10.18063/ijb.735
14. Fu M, Li J, Liu M, et al. Sericin/Nano-Hydroxyapatite Hydrogels Based on Graphene Oxide for Effective Bone Regeneration via Immunomodulation and Osteoinduction. *Int J Nanomedicine*. 2023;18:1875–1895. doi:10.2147/ijn.S399487
15. Li L, Pan C, Zhang X, et al. Efficacy of cementless porous tantalum tibial components versus cemented tibial components in primary total knee arthroplasty: A meta-analysis. *Medicine (Baltimore)*. Apr 5 2024;103(14):e37697. doi:10.1097/md.0000000000037697
16. Ji Y, Hou M, Zhang J, et al. Preparation and Properties of Partial-Degradable ZrO(2)-Chitosan Particles-GelMA Composite Scaffolds. *Polymers (Basel)*. Oct 9 2022;14(19)doi:10.3390/polym14194233
17. Zheng C, Attarilar S, Li K, et al. 3D-printed HA15-loaded β-Tricalcium Phosphate/Poly (Lactic-co-glycolic acid) Bone Tissue Scaffold Promotes Bone Regeneration in Rabbit Radial Defects. *Int J Bioprint*. 2021;7(1):317. doi:10.18063/ijb.v7i1.317
18. Pouroutzidou GK, Papadopoulou L, Lazaridou M, et al. Composite PLGA-Nanobioceramic Coating on Moxifloxacin-Loaded Akermanite 3D Porous Scaffolds for Bone Tissue Regeneration. *Pharmaceutics*. Mar 2 2023;15(3)doi:10.3390/pharmaceutics15030819
19. Tang Z, Li X, Tan Y, Fan H, Zhang X. The material and biological characteristics of osteoinductive calcium phosphate ceramics. *Regen Biomater*. 2017;5(1):43–59. doi:10.1093/rb/rbx024
20. Ma C, de Barros NR, Zheng T, et al. 3D Printing and Surface Engineering of Ti6Al4V Scaffolds for Enhanced Osseointegration in an In Vitro Study. *Biomimetics (Basel)*. Jul 10 2024;9(7)doi:10.3390/biomimetics9070423
21. Luo L, Wen Z, Hong G, Chen S. Reliable lateral Zn deposition along (002) plane by oxidized PAN separator for zinc-ion batteries. *RSC Adv*. Nov 30 2023;13(50):34947–34957. doi:10.1039/d3ra05177c
22. Li M, Zhao Z, Yi J. Biomaterials Designed to Modulate Reactive Oxygen Species for Enhanced Bone Regeneration in Diabetic Conditions. *J Funct Biomater*. Aug 8 2024;15(8)doi:10.3390/jfb15080220
23. Dutta SD, Ganguly K, Patil TV, Randhawa A, Lim KT. Unraveling the potential of 3D bioprinted immunomodulatory materials for regulating macrophage polarization: State-of-the-art in bone and associated tissue regeneration. *Bioact Mater*. Oct 2023;28:284–310. doi:10.1016/j.bioactmat.2023.05.014
24. Novella I, Rupaedah B, Eddy DR, et al. The Influence of Polyvinyl Alcohol Porogen Addition on the Nanostructural Characteristics of Hydroxyapatite. *Materials (Basel)*. Sep 20 2023;16(18)doi:10.3390/ma16186313
25. Rasmussen AN, Thomsen BL, Christensen JB, Petersen JC, Lassen M. Quartz-Enhanced Photoacoustic Spectroscopy Assisted by Partial Least-Squares Regression for Multi-Gas Measurements. *Sensors (Basel)*. Sep 20 2023;23(18)doi:10.3390/s23187984
26. Han L, Peng K, Qiu LY, et al. Hitchhiking on Controlled-Release Drug Delivery Systems:

ACCEPTED PAPER

Opportunities and Challenges for Cancer Vaccines. *Front Pharmacol*. 2021;12:679602. doi:10.3389/fphar.2021.679602
27. Frent OD, Vicas LG, Duteanu N, et al. Sodium Alginate-Natural Microencapsulation Material of Polymeric Microparticles. *Int J Mol Sci*. Oct 11 2022;23(20)doi:10.3390/ijms232012108
28. Zhang B, Bai M, Yang M, et al. Injectable nanocomposite hydrogel for localized precision delivery of dexamethasone after traumatic brain injury: dual modulation of neuroinflammation and blood-brain barrier restoration. *J Transl Med*. May 23 2025;23(1):579. doi:10.1186/s12967-025-06528-w
29. Luo Z, Ma J, Wang Y, et al. Application of Mg-MOF-loaded gelatin microspheres with osteogenic, angiogenic, and ROS scavenging capabilities in bone defect repair. *Int J Biol Macromol*. Nov 2024;280(Pt 2):135721. doi:10.1016/j.ijbiomac.2024.135721
30. Zhang X, Chen Q, Mao X. Magnesium Enhances Osteogenesis of BMSCs by Tuning Osteoimmunomodulation. *Biomed Res Int*. 2019;2019:7908205. doi:10.1155/2019/7908205
31. Zhou Y, Yang Y, Liu R, et al. Research Progress of Polydopamine Hydrogel in the Prevention and Treatment of Oral Diseases. *Int J Nanomedicine*. 2023;18:2623–2645. doi:10.2147/ijn.S407044
32. Hao J, Du L, He Y, Wu C. Bioceramic Surface Topography Regulating Immune Osteogenesis. *BME Front*. 2025;6:0089. doi:10.34133/bmef.0089
33. Hou Z, Liu X, Zhang X, Tan J, Liu X. Construction of Silver-Calcium Micro-Galvanic Cell on Titanium for Immunoregulation Osteogenesis. *BME Front*. 2025;6:0173. doi:10.34133/bmef.0173
34. Zeng M, Huang Z, Cen X, et al. Biomimetic Gradient Hydrogels with High Toughness and Antibacterial Properties. *Gels*. Dec 21 2023;10(1)doi:10.3390/gels10010006
35. Mulvee M, Vasiljevic N, Mann S, Patil AJ. Stimuli-Responsive Nucleotide-Amino Acid Hybrid Supramolecular Hydrogels. *Gels*. Sep 17 2021;7(3)doi:10.3390/gels7030146
36. Wang X, Liu W, Yu X, et al. Advances in surface modification of tantalum and porous tantalum for rapid osseointegration: A thematic review. *Front Bioeng Biotechnol*. 2022;10:983695. doi:10.3389/fbioe.2022.983695
37. Xiao L, Li Y, Geng R, et al. Polymer composite microspheres loading (177)Lu radionuclide for interventional radioembolization therapy and real-time SPECT imaging of hepatic cancer. *Biomater Res*. Nov 4 2023;27(1):110. doi:10.1186/s40824-023-00455-x
38. Danchuk O, Levchenko A, da Silva Mesquita R, et al. Meeting Contemporary Challenges: Development of Nanomaterials for Veterinary Medicine. *Pharmaceutics*. Sep 15 2023;15(9)doi:10.3390/pharmaceutics15092326
39. Zhao D, Cheng L, Lu F, et al. Design, fabrication and clinical characterization of additively manufactured tantalum hip joint prosthesis. *Regen Biomater*. 2024;11doi:10.1093/rb/rbae057
40. Li J, Cheng L, Yang J, et al. Study on the performance of selected laser melting porous Ta scaffolds with different porosities used as orthopedics implant biomaterial. *Journal of Materials Research and Technology*. 2025/05/01/ 2025;36:9320–9332. doi:https://doi.org/10.1016/j.jmrt.2025.05.195
41. Gao H, Yang J, Jin X, et al. Porous tantalum scaffolds: Fabrication, structure, properties, and orthopedic applications. *Materials & Design*. 2021/11/15/ 2021;210:110095. doi:https://doi.org/10.1016/j.matdes.2021.110095
42. Yang J, Gao H, Zhang D, et al. Static Compressive Behavior and Material Failure

ACCEPTED PAPER

Mechanism of Trabecular Tantalum Scaffolds Fabricated by Laser Powder Bed Fusion-based Additive Manufacturing. *IJB*. 2021;8(1)doi:10.18063/ijb.v8i1.438
43. Lin Z, Wu J, Qiao W, et al. Precisely controlled delivery of magnesium ions thru sponge-like monodisperse PLGA/nano-MgO-alginate core-shell microsphere device to enable in-situ bone regeneration. *Biomaterials*. Aug 2018;174:1–16. doi:10.1016/j.biomaterials.2018.05.011
44. Ma L, Cheng S, Ji X, et al. Immobilizing magnesium ions on 3D printed porous tantalum scaffolds with polydopamine for improved vascularization and osteogenesis. *Mater Sci Eng C Mater Biol Appl*. Dec 2020;117:111303. doi:10.1016/j.msec.2020.111303
45. Xu J, Wu D, Ge B, et al. Selective Laser Melting of the Porous Ta Scaffold with Mg-Doped Calcium Phosphate Coating for Orthopedic Applications. *ACS Biomater Sci Eng*. Mar 11 2024;10(3):1435–1447. doi:10.1021/acsbiomaterials.3c01503
46. Liu W, Wang T, Yang C, et al. Alkaline biodegradable implants for osteoporotic bone defects--importance of microenvironment pH. *Osteoporos Int*. Jan 2016;27(1):93–104. doi:10.1007/s00198-015-3217-8
47. Siffert RS. The role of alkaline phosphatase in osteogenesis. *J Exp Med*. May 1951;93(5):415–26. doi:10.1084/jem.93.5.415
48. Gu L, Huang R, Ni N, et al. Mg-Cross-Linked Alginate Hydrogel Induces BMSC/Macrophage Crosstalk to Enhance Bone Tissue Regeneration via Dual Promotion of the Ligand-Receptor Pairing of the OSM/miR-370-3p-gp130 Signaling Pathway. *ACS Appl Mater Interfaces*. Jun 19 2024;16(24):30685–30702. doi:10.1021/acsami.4c02795
49. Zhao Z, Li G, Ruan H, et al. Capturing Magnesium Ions via Microfluidic Hydrogel Microspheres for Promoting Cancellous Bone Regeneration. *ACS Nano*. Aug 24 2021;15(8):13041–13054. doi:10.1021/acsnano.1c02147
50. Wang M, Chen F, Wang J, et al. Calcium phosphate altered the cytokine secretion of macrophages and influenced the homing of mesenchymal stem cells. *J Mater Chem B*. Aug 7 2018;6(29):4765–4774. doi:10.1039/c8tb01201f
51. Gu P, Zhu Z, Xiao X, et al. Actively Infiltrative Micro/Nanochannels Propel Cell Migration-to-Mechanoactivation Transition for Centralized Osteogenesis. *ACS Nano*. Sep 2 2025;19(34):31092–31106. doi:10.1021/acsnano.5c09462
52. Chen KH, Chen CY, Wang WR, et al. Development and evaluation of an injectable ChitHCl-MgSO(4)-DDA hydrogel for bone regeneration: In vitro and in vivo studies on cell migration and osteogenesis enhancement. *Biomater Adv*. Oct 2024;163:213963. doi:10.1016/j.bioadv.2024.213963
53. Zhao D, Witte F, Lu F, et al. Current status on clinical applications of magnesium-based orthopaedic implants: A review from clinical translational perspective. *Biomaterials*. Jan 2017;112:287–302. doi:10.1016/j.biomaterials.2016.10.017
54. Cheng P, Han P, Zhao C, et al. High-purity magnesium interference screws promote fibrocartilaginous entheses regeneration in the anterior cruciate ligament reconstruction rabbit model via accumulation of BMP-2 and VEGF. *Biomaterials*. Mar 2016;81:14–26. doi:10.1016/j.biomaterials.2015.12.005
55. Zhao N, Zhu D. Collagen self-assembly on orthopedic magnesium biomaterials surface and subsequent bone cell attachment. *PLoS One*. 2014;9(10):e110420. doi:10.1371/journal.pone.0110420
56. Zhang X, Zu H, Zhao D, et al. Ion channel functional protein kinase TRPM7 regulates Mg ions to promote the osteoinduction of human osteoblast via PI3K pathway: In vitro

ACCEPTED PAPER

simulation of the bone-repairing effect of Mg-based alloy implant. *Acta Biomater*. Nov 2017;63:369–382. doi:10.1016/j.actbio.2017.08.051
57. Chen S, Liu F, Xin H, et al. Boosting MRSA Infectious Osteoporosis Treatment: Mg-Doped Nanofilm on Vacancy-Enriched TiO2 Coating for Providing In Situ Sonodynamic Bacteria-Killing and Osteogenic Alkaline Microenvironment. Advanced Functional Materials. 2024;34(11):2311965. doi:https://doi.org/10.1002/adfm.202311965
58. Avery D, Morandini L, Celt N, et al. Immune cell response to orthopedic and craniofacial biomaterials depends on biomaterial composition. Acta Biomater. Apr 15 2023;161:285–297. doi:10.1016/j.actbio.2023.03.007
59. Liu A, Liao H, Zhang X, et al. A novel tantalum scaffold promoting osteoporotic osseointegration by controlled immune regulation. IJB. 2025;11(2)doi:10.36922/ijb.8595
60. Sun Q, Zhou Y, Zhang A, et al. The immunomodulatory effects and mechanisms of magnesium-containing implants in bone regeneration: A review. Journal of Magnesium and Alloys. 2024;12(07):2695–2710. doi:https://doi.org/10.1016/j.jma.2024.05.011
61. Bessa-Gonçalves M, Ribeiro-Machado C, Costa M, et al. Magnesium incorporation in fibrinogen scaffolds promotes macrophage polarization towards M2 phenotype. Acta Biomater. Jan 1 2023;155:667–683. doi:10.1016/j.actbio.2022.10.046

ACCEPTED PAPER